Computers & Fluids 119 (2015) 47–57

Contents lists available at ScienceDirect

Computers & Fluids

journal homepage: www.elsevier.com/locate/compfluid

# Computational study of non-ideal and mildly-unstable detonation waves

A. Sow [a], A. Chinnayya [b], A. Hadjadj [a,*]

[a] CORIA-UMR 6614, Normandie University, CNRS-University & INSA of Rouen, 76800 St Etienne du Rouvray, France
[b] Institut PPRIME, CNRS UPR 3346, ENSMA & University of Poitiers, 86961 Futuroscope-Chasseneuil Cedex, France

ARTICLE INFO

*Article history:*
Received 20 November 2014
Received in revised form 26 May 2015
Accepted 23 June 2015
Available online 2 July 2015

*Keywords:*
WENO
HLLC
Shock detector
Strang splitting
Non-ideal detonation
Instabilities

ABSTRACT

This paper deals with some salient features of numerical detonation modeling, whose shock dynamics exhibits mildly oscillations behavior. The study is based on the integration of the hyperbolic equations with source terms, using a fifth-order Weighted Essentially Non-Oscillatory (WENO) scheme for the convective flux and a third-order Runge–Kutta scheme for time advancement. Strang's splitting technique is used for the integration of the source terms. The computations are performed for both stable and mildly unstable detonation waves. The study shows that the rate of convergence depends on the smoothness of the solution and that in presence of strong detonation waves, the accuracy is much lower than commonly believed. To improve the computation accuracy, a simple algorithm for shock detection is proposed along with a chemical activator for weak activation energies. A mesh refinement is also employed to achieve high resolution computations. It is found that a resolution of 66 points per half reaction zone is required to correctly capture the main structure of the detonation front and the associated flow instabilities. Examples are carried out to show that the proposed model yield accurate results. In particular, as the friction and the heat losses increase, the mean detonation velocity decreases and a series of period-doubling self sustained oscillations appears. It is also found that non-adiabatic conditions play a crucial role on the dynamics of the shock front, by enhancing the fluctuations. This aspect should be properly accounted for when dealing with multi-dimensional detonations.



## 1. Introduction

A detonation wave is a supersonic combustion where a leading shock is strongly coupled with a reaction zone, in which a chemical decomposition occurs until the fresh mixture is completely converted into products. The strong coupling between the shock and the reaction zone makes the detonation wave self-similar. The minimum self-sustained detonation velocity is the ideal Chapman–Jouguet (CJ) detonation speed. The inner structure of the detonation wave can be determined from the ZND (Zel'dovich, von Neumann, Döring) model, which relies on the steady one-dimensional Euler reactive formalism. For CJ detonations, the end of the reaction zone is characterized by the sonic condition in the reference frame attached to the shock [1,2].

In the past, several authors have studied the dynamics of ideal one-dimensional detonations using a single-step Arrhenius model [3–6] by numerical means. These studies indicated that the activation energy ($E_a$) is the main parameter which controls the onset of the longitudinal instability for constant heat of reaction and specific heat ratio. For activation energies below a critical threshold $E_{a,c}$, the linear stability analysis shows the existence of a stable steady detonation structure. Above $E_{a,c}$, oscillatory modes emerge [7,4] making the detonation weakly then mildly unstable up to becoming chaotic through the Feigenbaum double-period scenario.

Moreover, with scale reduction the propagation of detonations is affected by the confinement effect, in contrast to the ideal case [8,2, Chap. 7]. The detonation velocity is therefore lower than the theoretical value due to the presence of solid walls. Following the pioneering work of Zel'dovich [8] which considers the momentum loss as the main mechanism responsible for the velocity deficit, Zhang and Lee [9] and later Dionne et al. [10] showed that the onset of the instability is not only triggered by $E_a$ but that drag forces are also important. Indeed, their numerical results indicated that the wall friction tends to enhance the natural detonation instabilities. They also pointed out that the stability limit is reduced in frictional detonations.

Furthermore, defining the sonic locus is a key issue in detonation. For steady state solutions, the generalized CJ criterion [2,11,12] can be used to determine the subsonic reaction zone. In unsteady detonations, Kasimov and Stewart [3] defined the sonic locus as a separatrix of the family of forward characteristics. Another important aspect in detonation problems is the dynamics of the leading shock which can be seen as a signature

* Corresponding author.
*E-mail address:* hadjadj@coria.fr (A. Hadjadj).

http://dx.doi.org/10.1016/j.compfluid.2015.06.027
0045-7930/

of different non-stationary events appearing in the subsonic reactive zone.

From a numerical view point, Romick et al. [13] have indicated that a shock-capturing method retrieves the main features of the detonation front dynamics with much finer resolution compared to the shock-fitting technique [14]. In the case of weakly and mildly unstable detonations, Bourlioux et al. [15] used a shock-tracking technique. However, the issue of numerical convergence remains when an "explosion within explosion occurs", and when secondary fronts form within the reaction zone and overtake the leading shock [16]. When using a shock-capturing technique, a criterion for determining the shock location is required. For example, Colella [17] for inert strong shocks and later Quirk [18] for detonation waves, used an empirical shock indicator based on the local relative pressure jump. Although, their criterion is well designed, it seems to be problem dependent. Recently, Yee et al. [19] used a minmod-like shock indicator. Their paper presents a state-of-art review of split and unsplit strategies. Spurious numerical solutions are reported when under-resolved computations are performed, as deflagration takes place within the numerical shock layer. Several numerical schemes are compared, as well as the extension to chemistry of the well-balanced strategy, which was primarily designed to deal with specific issues associated with stiff geometric source terms [20]. Lately, Menikoff and Shaw [21] proposed a shock sensor based on the Hugoniot jump conditions for condensed phase-detonations, which is independent of the numerical dissipation. As the numerical scheme is entropy-positive, the shock sensor is based on the relative position of the thermodynamic states within the shock numerical layer as compared to the Hugoniot curve. This criterion is however dependent on the state upstream of the shock. Thus no burning occurs within the numerical shock width [22]. Activation of chemistry thereby occurs only after the shock passage, which is in accordance with the ZND theory. This is also a common prescription to ensure the correct detonation speed [23], even for underresolved resolution of the reaction zone. Timmes et al. [24] show that the strength of the cellular features, which depend on the detonation instabilities are resolution-dependent. Papatheodore and Messer [23] also point out that the numerical prohibition of burning within the numerical shock can affect the capabilities of the numerical method to capture the associated flow instabilities.

Moreover, the use of higher order schemes for the hyperbolic part is much more suitable to properly capture the period of the shock oscillation, while a second-order scheme can be sufficient to retrieve the peak pressure. As shown in Hwang et al. [6], higher-order ENO schemes (higher than three) are able to predict the oscillation period more accurately for a given mesh spacing compared to second-order schemes. The former schemes achieve better convergence behavior. Yet, they indicate that higher-order schemes can achieve the correct peak pressure with a relatively coarse mesh. Indeed, in detonation computations, it seems important to resolve as accurately as possible the reaction zone, which contains a wide variety of smooth fine scales, which has been one of the scopes of the design of the WENO schemes [33]. Indeed, the fluctuations of the leading shock give rise to a train of characteristic as well as entropy waves. In turn, they modify the state sensitive reaction-rate and the reaction zone behaves like a non-linear oscillator [26]. For example, during the deceleration of the leading shock, a reaction front and a pressure buildup will arise and will then overtake the leading shock. It is thus desirable not to smooth out the peak overpressure, as would do any TVD scheme, in order to capture the time dynamics of this leading shock. In another context, the space–time diagram and the corresponding shock to detonation transition have been shown by Xu et al. [27] to be more accurately captured with a fifth-order WENO numerical scheme compared to a second-order scheme. In this study, we use the usual Strang splitting to couple the integration of the hyperbolic operator with that of the chemistry, as recalled by Yee et al. [19]. Moreover, the latter authors, based on extensive numerical studies between fifth and second-order schemes have concluded that the less dissipative scheme, the better for very coarse grid, in particular as for the shock location. This is of particular interest for our study. Thus the use of high-order numerical schemes is recommended, when dealing with detonation instabilities.

We then focus on the inherent numerical resolution needed in order to capture this increase of instabilities. More specifically, we investigate the dynamics of the von-Neumann spike, which is the post-shock state characterized by a local extremum in the flow. It is therefore the most difficult feature to capture. The effect of the mesh refinement and that of the shock indicator versus the activation energy are studied. The objective is to highlight the numerical features needed to apply the non-linear analysis of Ng et al. [4] to the post-shock state and to determine the mean sonic locus [25] which accounts for the presence of the fluctuations in the reaction zone, in the case where the detonation non-ideality comes from the momentum and heat losses.

This paper is organized as follows. The governing equations as well as the post-processing procedure leading to the definition of the mean detonation structure and the sonic locus are presented in Section 2. The numerical procedure is given in Section 3. Results and discussions are presented in Section 4. The main conclusions are drawn in Section 5.

## 2. Governing equations

The flow is governed by the one-dimensional unsteady reactive Euler equations with friction and heat loss (Zel'dovich model). The system is cast into the following conservative form

$$U_\tau + F_\chi = S \tag{1}$$

where $U = (\rho, \rho v, \rho E, \rho Y)$ is the conservative vector, $F = (\rho v, \rho v^2 + p, \rho E v + p v, \rho Y v)$ the convective flux, and $S = (0, f, \dot{q}_{th} + v f, \dot{\omega})$ are the source terms. $\tau$ and $\chi$ are the coordinates in the laboratory frame. $\rho, v, p$ and $E$ denotes density, velocity, total energy $E = e + v^2/2$, respectively. $e = p/(\gamma - 1)\rho + Yq$ is the internal energy, $Y$ the reactant mass fraction, $q$ the heat of reaction, and $\gamma$ the polytropic coefficient. $f = -c_f \rho |v| v/2d$ is the drag force, $c_f$ the skin friction. The heat loss is $\dot{q}_{th} = -h_c(T - T_w)/2d$, where $h_c = \rho c_p |v| c_f/2$ is obtained via the Reynolds analogy [11]. $c_p, T, T_w$ and $d$ are the heat capacity, the static temperature, the wall temperature and the diameter of the tube, respectively. A simple Arrhenius exothermic source term $\dot{\omega} = -\mathcal{A}\rho Y \exp(-E_a/RT)$ is used to model the chemical reaction. Both reactants and products are considered as perfect gases, having the same molecular mass and specific heats. $\mathcal{A}$ and $E_a$ denote the pre-exponential factor and the activation energy, respectively. The chemical source term is set to zero when the mass fraction goes below a threshold of $10^6$. In Sow et al. [30], we show that the work of friction which is expressed by the product of friction force by the velocity implies that the only source of entropy production is due to the irreversible chemical reaction. In the present study, the thermal heat transfer should be added as another source of entropy production. This difference with the more classical formulation has been done in order to underline the extra-deficit of velocity of the detonation front and its dynamics, which are inferred by the presence of fluctuations. Indeed, the right-hand side of the mean Gibbs relation would imply only quantities with fluctuations, whereas in the other case, there will be terms relative to mean quantities, hiding the physics. When a metric $\xi_\chi$, which will be defined in Section 3.2, is used the governing equation can be cast in the following form

$$U_\tau + \xi_\chi F_\xi = S \tag{2}$$

We present in the following the steady Zel'dovich–von Neumann–Döring (ZND) solution and the mean structure of the detonation reaction zone.

### 2.1. Steady ZND solution

The set of equations for steady state is given by (see Zhang and Lee [9] for more details)

$$\frac{d}{dx}(\rho u) = 0 \tag{3a}$$

$$\frac{d}{dx}(\rho u^2 + p) = f \tag{3b}$$

$$\frac{d}{dx}(\rho E u + p u) = u f + \dot{q}_{th} \tag{3c}$$

$$\frac{d}{dx}(\rho u Y) = \dot{\omega} \tag{3d}$$

where $x$ and $u$ denote the distance from the leading shock front and the fluid particles velocity in the reference of the shock, respectively. The so-called Master Equation ($ME_{ZND}$), which is the generalized CJ solution, is obtained after some algebraic manipulations of Eqs. (3a)–(3d)

$$\frac{du}{dx} = \frac{\phi_{ZND}}{\rho c^2 (1 - M^2)} \tag{4}$$

where $\phi_{ZND} = -(\gamma - 1) q \dot{\omega} - u f + (\gamma - 1)\dot{q}_{th}$. $M = u/c$ is the Mach number and $c$ the thermodynamic speed of sound. The zone between the incident shock and the sonic location defines the steady subsonic reaction zone. The sonic locus is obtained when the numerator (thermicity) and the denominator (sonicity) of Eq. (4) go simultaneously to zero.

Eqs. (3a)–(3d) are solved with a shooting method which is an iterative technique based on the detonation velocity, $D$. The main steps of the shooting algorithm can be summarized as follows:

1. Give an arbitrary detonation velocity to start the iterative procedure.
2. Solve the set of Eqs. (3a)–(3d) using a second-order Euler method.
3. Check if the thermicity and the sonicity go simultaneously to zero. Three cases are possible:
   (a) the thermicity goes to zero and the sonicity remains greater than zero meaning that the given velocity corresponds to that of an overdriven detonation. The initial detonation velocity is then decreased,
   (b) the thermicity is different from zero and the sonicity goes to zero, the numerical solution is not physical (as derivatives become infinite), the detonation velocity is increased,
   (c) both thermicity and sonicity go to zero. The detonation velocity is the desired one, which ends the iteration process.

The criterion for the thermicity to be zero is the following

$$Y + \frac{u f + (\gamma - 1)\dot{q}_{th}}{(\gamma - 1) q \mathcal{A} \rho \exp(-E_a/RT)} < \epsilon_1 \tag{5}$$

In all the calculations, $\epsilon_1 < 10^{-8}$—$10^{-6}$, with $\Delta x \approx 1$—$0.01\mu$m. The steady state solution obtained here is to be compared to the numerical solution obtained from the direct simulations of Eq. (2). The criterion for the sonicity to be zero is

$$|1 - M^2| < \epsilon_1 \tag{6}$$

### 2.2. Mean solution

The unsteady solution is obtained by resolving Eq. (2). Then the numerical results are post-treated in the instantaneous shock-attached frame to define the mean structure of the detonation wave. In contrast with Gamezo et al. [28] and Radulescu et al. [29], the Favre-averaged procedure, which is detailed in [30] is conditioned by the position of the shock. Based on this analysis, a new Favre-averaged Master Equation (ME) defining the mean sonic locus has been obtained

$$\frac{d\tilde{u}}{dx} = \frac{\tilde{\phi}}{\bar{\rho}\tilde{c}_T^2 (1 - \tilde{M}_T^2)} \tag{7}$$

where $\tilde{c}_T^2 = \tilde{c}^2 + c_t^2$ is the effective speed of sound, $\tilde{c}^2 = \gamma \bar{p}/\bar{\rho}$ is the thermodynamic speed of sound and $\tilde{c}_t^2 = 6k$ is the speed related to the mechanical fluctuations energy $k = \widetilde{u''^2}/2$. The associated effective Mach number is $\tilde{M}_T = \tilde{u}/\tilde{c}_T$. $\tilde{\phi}$ is the mean thermicity, which is the sum of the following contributions

$$\tilde{\phi}_{chem} = -(\gamma - 1) q \overline{\dot{\omega}}$$

$$\tilde{\phi}_{visc} = (\gamma - 1)\overline{u f} - \gamma \tilde{u} \bar{f}$$

$$\tilde{\phi}_{th} = (\gamma - 1)\overline{\dot{q}_{th}}$$

$$\tilde{\phi}_{acc} = \gamma \tilde{u} \overline{\rho \dot{D}} - (\gamma - 1)\overline{\rho \dot{D} u},$$

$$\tilde{\phi}_{fluc} = -3\frac{d}{dx}\overline{p' u''} - \frac{d}{dx}\overline{\rho u''^3} + (3 - \gamma)\left(-\overline{u''}\frac{d\bar{p}}{dx} + \overline{p'\frac{du''}{dx}} + \overline{u'' f} - \overline{\rho \dot{D} u''}\right) - \gamma \frac{d}{dx}(\bar{p}\overline{u''})$$

where $\tilde{\phi}_{chem}$ represents the exothermic contribution due to the chemical heat-release while $\tilde{\phi}_{visc}$ reflects the effect of the drag forces and $\tilde{\phi}_{th}$ the heat losses. $\tilde{\phi}_{acc}$ and $\tilde{\phi}_{fluc}$ are two news contributions due to the effects of the acceleration of the shock front and the mechanical fluctuations.

The above cited contributions will be evaluated by post-processing the Direct Numerical Simulation (DNS) of the numerical resolution of Eq. (2).

## 3. Numerical procedure

The details of the high order shock-capturing scheme as well as the numerical setup are given here. The outline of the WENO5-HLLC spatial discretization and the temporal third-order Runge–Kutta scheme are presented in [31]. We will present here the Strang's splitting resolution method and the computational grid. The numerical mean procedure will also be presented.

Eq. (2) is solved using the fractional step approach [32,12]. Without loss of generality and for simplicity, the fractional step method is briefly presented. At first, the homogenous part of Eq. (2) is solved

$$U_\tau + \xi_\chi F_\xi = 0 \tag{8}$$

with the initial condition $U^n$ over a time step $\Delta t^n$, to obtain the temporary solution $U^*$. The WENO approximation is here applied to $F_\xi$. As $\xi$ is smooth enough, discrete conservation still holds [33]. The discrete numerical operator, which integrates the hyperbolic part of the system of equations is denoted $\mathcal{L}_\mathcal{H}$. Thus $U^* = \mathcal{L}_\mathcal{H} U^n$. Then, in the second step, the source term operator is integrated

$$U_\tau = S \tag{9}$$

with the initial condition $U^*$. The discrete numerical operator is denoted $\mathcal{L}_\mathcal{S}$. In order to achieve an order of two, the Strang splitting is used instead of the previous Lie splitting. This achieves the coupling between the hydrodynamic solver and the source terms (see also [31,34]).

$$U^{n+1} = \mathcal{L}_\mathcal{S}(\Delta t^n/2)\mathcal{L}_\mathcal{H}(\Delta t^n)\mathcal{L}_\mathcal{S}(\Delta t^n/2)U^n \tag{10}$$

### 3.1. Integration of source terms

For the integration of the source terms a second-order method is used

$$U^{(1)} = U^n + \frac{\Delta t^n}{2}\mathcal{L}_s(U^n, \Delta t/2) \tag{11a}$$

$$U^* = U^n + \Delta t^n \mathcal{L}_s(U^{(1)}, \Delta t) \tag{11b}$$

where $\mathcal{L}_s$ is the discrete source term operator. When $\mathcal{L}_s = S$, then the integration is that of the Euler forward method. An exponential integration can also be used as in [31]. For example, if the following time scale $\tau = -U/S$ is defined from the source term of the reactant and is hold constant during the time step, we get the exponential integration [35] and $\mathcal{L}_s = U(\exp(-\Delta t/\tau) - 1)$. The discrete source term for the products follows from the saturation constraint. The latter integration is more stable in the course of the chemical integration. In overall, we can write $U^* = \mathcal{L}_S(\Delta t^n)U^n$. In the following, the time step is imposed by the hyperbolic operator. As the objective is to determine the shock dynamics, the reaction zone can no longer be under-resolved.

The activation of the chemical reaction, occurring behind the leading front, is an important topic in detonation. For all of the considered cases in this paper, the chemical reaction is switched on only for

$$p/p_0 \geqslant 10 \text{ and } Y \geqslant 10^{-6} \tag{12}$$

Condition (12) (called after chemical activator) is imposed to ensure that only the shocked fluid particles will react [14]. As an indication,

$$M_{CJ} = \sqrt{(\gamma^2 - 1).\frac{q}{2c_0^2}} + \sqrt{(\gamma^2 - 1).\frac{q}{2c_0^2} + 1}$$

and

$$p_{CJ}/p_0 = \frac{1 + \gamma M_{CJ}^2}{1 + \gamma} \simeq 12.5$$

with $M_{CJ} \simeq 5$–$7$ and $\gamma = 1.2$. Of course, for condition (12) to be valid the search of the local pressure starts from the undisturbed flow to the shocked one.

### 3.2. Mesh generation

A fixed (time-independent) grid stretching technique based on Roberts' distribution [36] is used to improve the resolution near the shock front and in the reaction zone. This distribution is given by

$$\chi(\xi)/\chi_c = 1 + \sinh[\varsigma(\xi/L_i - \Lambda)]/\sinh(\varsigma\Lambda) \tag{13}$$

where $\chi_c$ is the point around which the mesh is clustered. $L_i$ is the length of the stretched area and $\varsigma$ a given positive parameter. $\Lambda$ is defined as

$$\Lambda = \frac{1}{2\varsigma}\ln\left[\frac{1 + (e^{\varsigma} - 1)(\chi_c/L_i)}{1 + (e^{-\varsigma} - 1)(\chi_c/L_i)}\right]$$

The set of equations is solved in the generalized coordinate system. Therefore, the transformation from the uniformly spaced grid in the computational domain $(0, \xi)$ to the non-uniformly spaced grid points in the physical domain $(0, \chi)$ is made through the mapping function

$$\xi = \xi(\chi) \text{ and } (\cdot)_\chi = \xi_\chi(\cdot)_\xi \tag{14}$$

where $\xi_\chi$ is the metrics obtained from Eq. (13) as

$$\xi_\chi = \frac{L_m \sinh(\varsigma\Lambda)}{\varsigma\chi_c\sqrt{1 + [\chi/\chi_c - 1]^2\sinh^2(\varsigma\Lambda)}}$$

The controlling parameter $\varsigma$ is given by the continuity condition between physical grid spacings. Consider for instance, a physical space which is divided into two sub-domains (see Fig. 1), with at left a non-uniform space of length $L_m$ with $N_m$ grid points and a uniform space with a length of $L_r$ and $N_r$ grid points at right. If the grid is tightened at $L_m$ (i.e. at $\chi_{N_m}$), the mapping function gives the smallest grid spacing in the non-uniform space $\Delta\chi_{min} = \chi_{N_m} - \chi_{N_{m-1}}$. Taking $\Delta\chi_{min}$ equal to the desired uniformly grid space $\Delta\chi_r = L_r/N_r = \Delta\chi_{min}$, will leads to the following condition on $\varsigma$

$$\Delta\chi_{min} = L_m\frac{\sinh(\varsigma/N_m)}{\sinh(\varsigma)} \tag{15}$$

$\varsigma$ is then obtained by solving Eq. (15) using the Newton–Raphson method.

In order to measure the von-Neumann spike pressure, it is worthwhile to know the shock position. Therefore a shock detector that can adequately characterize the shock movement is needed. In what follows, two types of shock indicator will be developed. In the following section, the fundamental steps of the construction of these shock indicators are recalled.

### 3.3. Shock indicators

Fluid particles that passed across the leading shock will undergo a significant pressure increase. This relative pressure jump is used by several authors [17,37] to estimate the position of the leading shock. Since a shock capturing scheme is used in this study, the location of high pressure gradient is first identified. After, a window of ten points is used to find the maximum pressure. In numerical formulation, the first step is to do a local search starting from the quiescent gases in order to locate the perturbed state. Then, the following condition is imposed to correct the shock position given by the first step

$$\frac{|p_{i-1}^n - p_i^n|}{p_{i-1}^n} > 10^{-2} \tag{16}$$

The new shock position is again improved by doing a maximum pressure research in a windows of ten points.

Another way to design a shock indicator is to use the Hugoniot curve as done recently by Menikoff and Shaw [21]. This method is based on the time-dependent Hugoniot curve defined as follows (see Fig. 2)

$$H(V(t), e(t)) = e(t) - e_0 - \frac{p(V(t), e(t)) + p_0}{2}(V(t) - V_0) \tag{17}$$

where $H, e$ and $V = 1/\rho$ are the time dependent Hugoniot curve, internal energy and volumetric fraction, respectively. The subscript 0 denotes the initial state. The shock state is determined by looking for a zero crossing in the case of compression waves following the leading shock. For downstream expansion waves, the shock position is indicated by a local minimum.

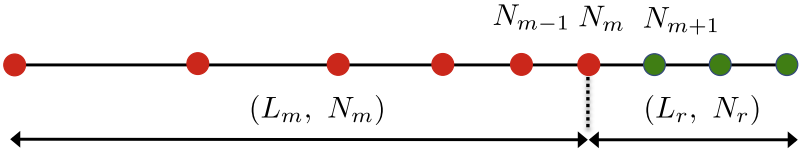


**Fig. 1.** Distribution of points of the physical space.

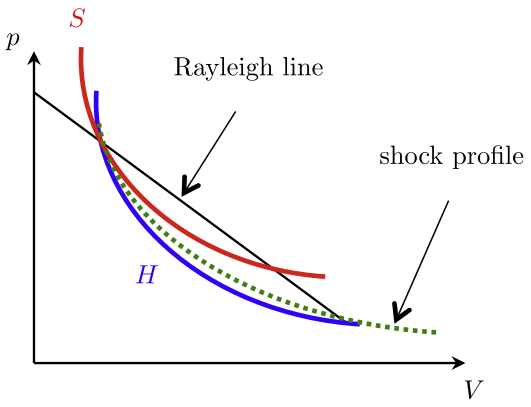


**Fig. 2.** Hugoniot curve ($H$), isentrope shocked state ($S$), shock profile, and Rayleigh line in $(p, V)$-diagram [21].

The algorithm for the shock detection is summarized below. First, Eq. (17) is discretized as

$$H_i^n = e_i^n - e_0 - \frac{p_i^n + p_0}{2}(V_i^n - V_0) \tag{18}$$

The position of the shock front is determined when the following conditions is satisfied

$$H_i^n H_{i-1}^n \leqslant 0 \text{ and } \left(H_i^n - H_{i-1}^n\right)\left(H_{i+1}^n - H_i^n\right) \leqslant 0 \tag{19}$$

or

$$H_{i+1}^n - 2H_i^n + H_{i-1}^n \geqslant 0 \tag{20}$$

### 3.4. Running average filter

The raw time-dependent data obtained using one of the above shock detection algorithm are corrupted by noise. The running average filter is then used to reduce the noise. The idea of the running average filter is simple. Each point in the output signal is generated by averaging a number of points from the input signal. This is translated mathematically as

$$p_s(i) = \frac{1}{N}\sum_{k=0}^{N-1} p_{sr}(i+k)$$

where $N$ is the number of points in the average. $p_{sr}$ and $p_s$ are the input and the output shock pressures, respectively.

### 3.5. Discrete mean procedure

Consider the temporal mean $\bar{\varphi}$ of a given variable $\varphi$

$$\bar{\varphi} = \lim_{\mathcal{T}\to\infty} \frac{1}{\mathcal{T}} \int_{t^0}^{t} \varphi \mathrm{d}t \tag{21}$$

where $\mathcal{T} = t - t^0$ is the sampling period and $t^0$ the starting time for integration. The first order discretization of Eq. (21) gives

$$\bar{\varphi} = \lim_{n\to\infty} \bar{\varphi}^n \quad \text{with} \quad \bar{\varphi}^n = \frac{1}{t^n - t^0}\sum_{m=n_i}^{n} \varphi^m (t^{m+1} - t^m) \tag{22}$$

Differentiating $\bar{\varphi}^{n+1}$ and $\bar{\varphi}^n$ leads to

$$\bar{\varphi}^{n+1}(t^{n+1} - t^0) - \bar{\varphi}^n(t^n - t^0) = \varphi^{n+1}(t^{n+1} - t^0)$$

which can be written into an incremental form

$$\bar{\varphi}^{n+1} = \bar{\varphi}^n - \frac{\Delta t^{n+1}}{t^{n+1} - t^0}(\bar{\varphi}^n - \varphi^{n+1}) \tag{23}$$

The initial $t^0$ is chosen at the end of the initial transients, when the mean detonation velocity has been stabilized. Moreover, this shortens the sampling period and fastens the convergence of the means. Note that the time step $\Delta t^n$ varies with time due to the dynamics of the leading shock.

## 4. Results and discussions

In this section, the numerical setup and the validation tests are first given. Secondly the influence of the mesh refinement is studied. Thirdly, the effect of grid resolution in the case of stable and unstable ideal detonations are evaluated. The last point of this section focus on the influence of the diameter reduction.

### 4.1. Problem setup

To quantify the relative effects of friction and heat losses on detonations, three tests cases are considered as reported in Table 1. For a validation purpose, an ideal detonation case is first considered. This case is denoted by $(A)$. In the second case denoted $(B)$, only friction is activated (adiabatic case) and in the third case denoted $(C)$, both friction and heat losses are activated. In each case, three tests can be performed using three different values of the activation energy. In the numerical tests, $\gamma = 1.2, q/RT_0 = 50, x_{1/2} = 0.265$ mm ($x_{1/2}$ is the half reaction zone for $E_a/RT_0 = 27$), $\mathcal{A} = 3.23 \times 10^{-7}$ 1/s, $p_0 = 0.1$ MPa and $T_0 = 300$ K. In this case, the critical activation energy $E_{a,c} \approx 25.26RT_0$. Zhang and Lee [9] and later Dionne et al. [10] showed that the onset of the instability is not only triggered by $E_a$ but that drag forces are also important. Indeed, their numerical results indicated that the wall friction tends to enhance the natural detonation instabilities. They also pointed out that the stability limit is reduced to $E_a = 22RT_0$ in frictional detonations.

**Table 1**
Cases of simulation.

| Cases | $f$ | $\dot{q}_{th}$ | Notation |
|---|---|---|---|
| Ideal detonation | Off | Off | $(A)$ |
| Frictional detonation | On | Off | $(B)$ |
| Detonation with friction and heat losses | On | On | $(C)$ |

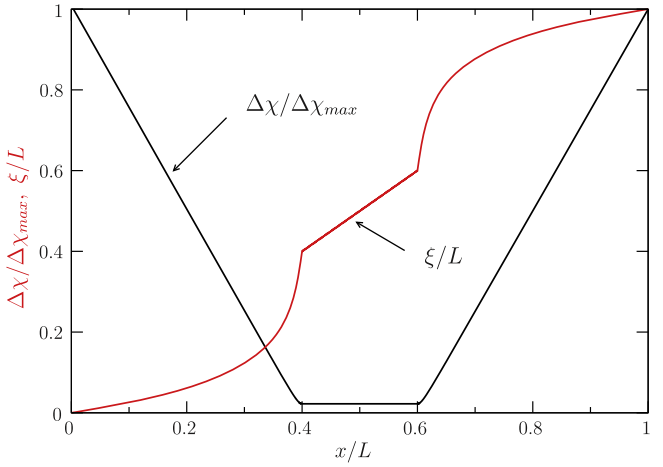


**Fig. 3.** Computational space $(\xi/L)$ as a function of the physical space $(x/L)$ and spatial mesh resolution distribution $(\Delta\chi/\Delta\chi_{max})$. $L$ is the total length of the computational domain and $\Delta\chi_{max}$ is the highest grid spacing.

In order to study the long-time behavior of the shock front, a negative inflow velocity is imposed at the right of the domain for the purpose of reducing memory and CPU consumption. The dimensionless length of the computational domain is $L^* = L/x_{1/2} = 189, L$ = 50 mm with at least a total of 3500 grid points (see Fig. 3). A fine and uniformly spaced mesh of at least 66 pts/$x_{1/2}$ is used to capture the shock front and the reaction zone. The mesh is then stretched in the upstream region (unburnt gas) and in the downstream (Zel'dovich–Taylor expansion waves) to allow the flow relaxing towards the far-field boundary conditions. Mean and fluctuating quantities are sampled and extracted over more than 30 cycles of shock movement which necessitate 96 h CPU on a MAC cluster.

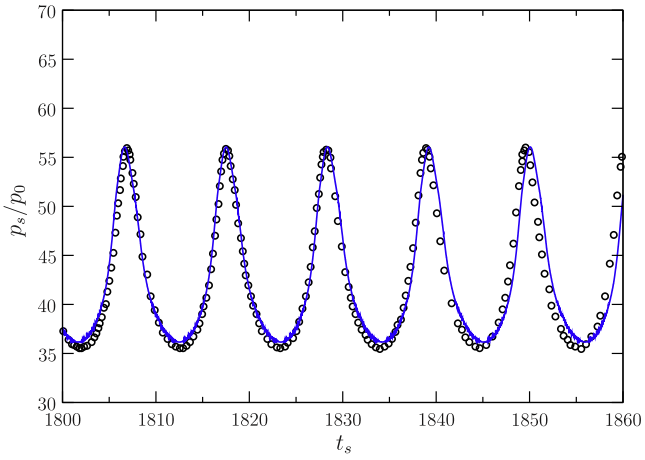


**Fig. 4.** Comparison of the peak pressure histories of current solution (line) and Ng et al. [4] (circles) numerical data. Ideal case at $E_a/RT_0 = 27$. $t_s = t\sqrt{RT_0}/x_{1/2}$.

### 4.2. Validation tests

These validation tests are taken from Ng et al. [4] within the frame of ideal unstable detonations. The first test deals with $E_a = 27RT_0$. Results obtained are depicted in Fig. 4. Good agreement between numerical results is shown. Validation tests are also conducted by increasing $E_a$. As mentioned by Ng et al. [4] among other authors two, four, and eight modes are obtained (in the case of ideal detonation) for $E_a = 27.40RT_0, E_a = 27.80RT_0$ and $E_a = 27.82RT_0$, respectively. These successive bifurcations from two-period to four-period and further from four-period to eight-period are correctly reproduced as shown in Fig. 5. In order to extract the physical signal, a running average procedure with a length of average of 601 points is applied to the raw results which have to be corrected from the numerical noise (see Section 3.4).

### 4.3. Influence of the chemical activator

By simulating stable ideal detonation waves, the influence of the chemical activator is evaluated. In the first simulation $E_a = 10RT_0$, two tests are performed. One is computed without chemical activator and the other with the chemical activator as

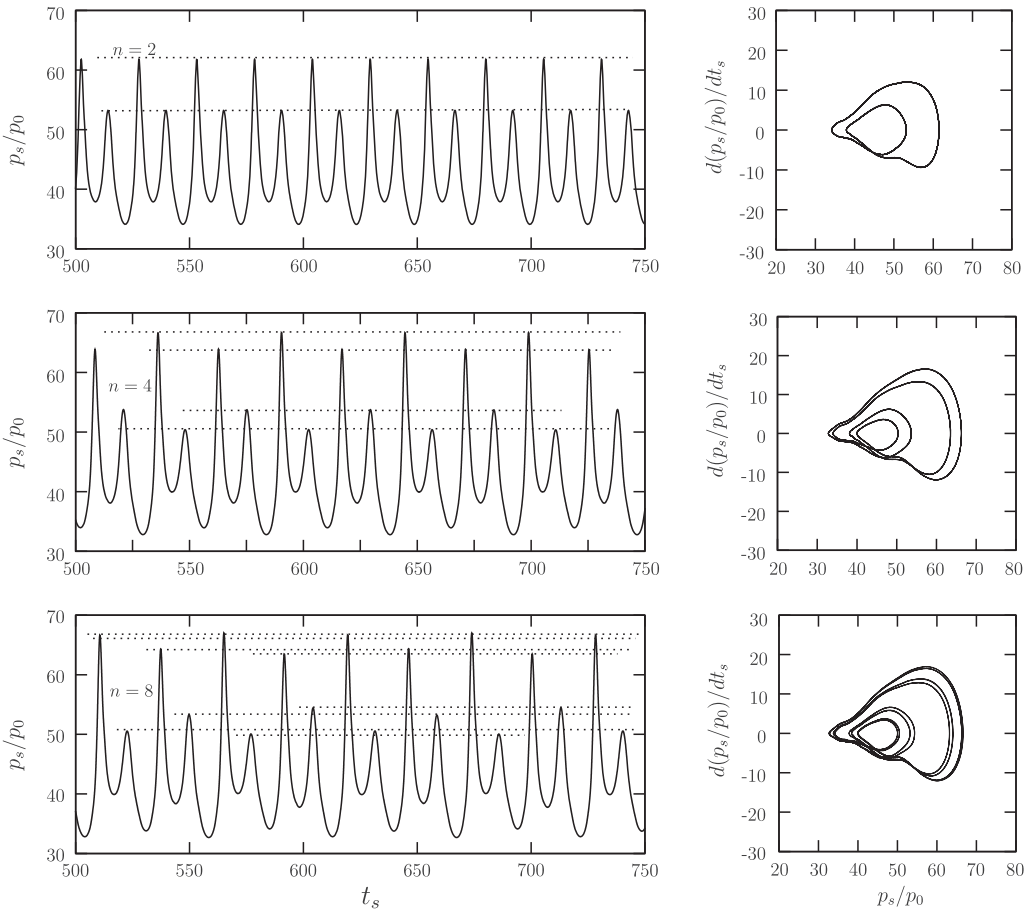


**Fig. 5.** Shock pressure $p_s$ history (left) and corresponding limit cycle (right) showing different modes of oscillations for $E_a = 27.40RT_0$ (2 modes), $E_a = 27.80RT_0$ (4 modes), and $E_a = 27.82RT_0$ (8 modes). $t_s = t\sqrt{RT_0}/x_{1/2}$.

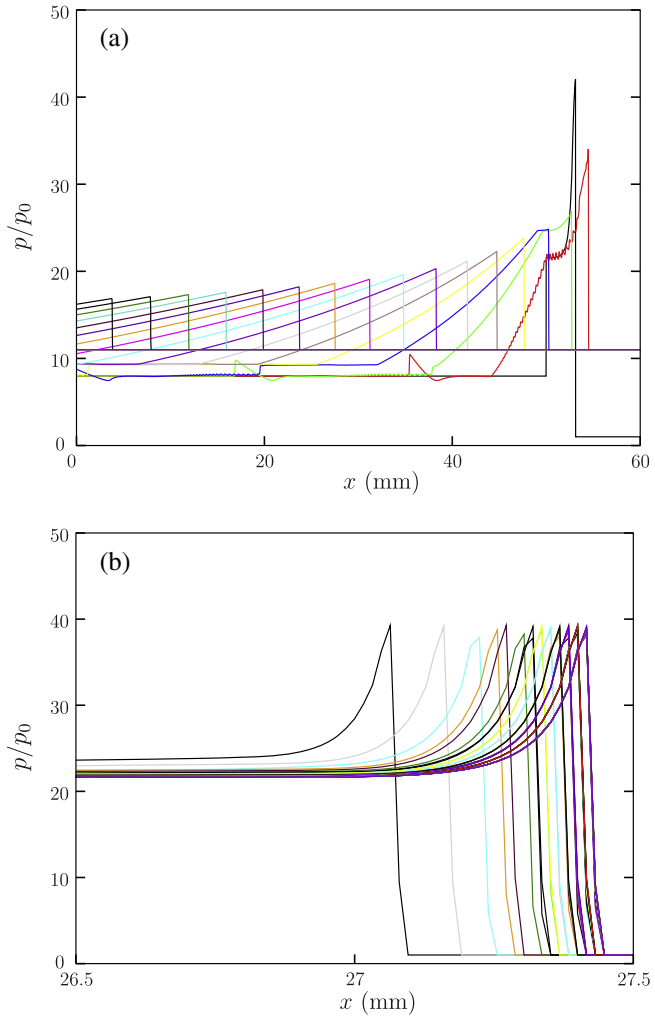


**Fig. 6.** Pressure profiles at different times for $E_a = 10RT_0$ in the case of ideal detonation. (a) Results computed without condition (12), the detonation fails and (b) result obtained using condition (12), the detonation is sustained. $\Delta\chi_r = 16$ μm.

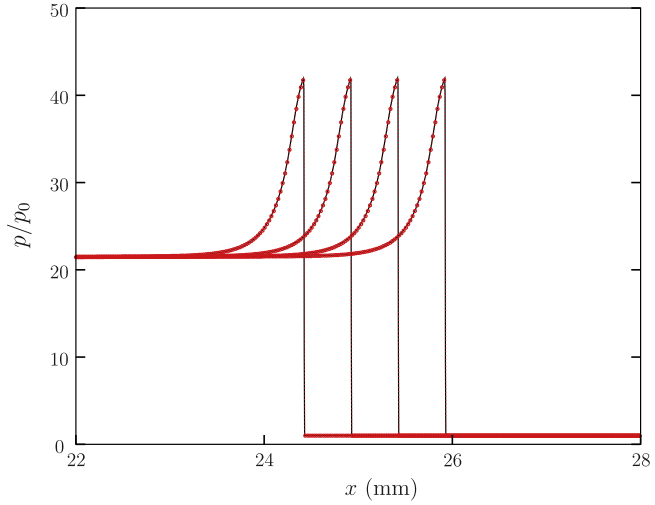


**Fig. 7.** Pressure profiles at different times for $E_a = 22RT_0$ in the case of ideal detonation. Lines represent computed results without condition (12) and symbols results obtained with condition (12).

depicted in Fig. 6. Results indicated that without chemical activator the detonation fails after initiation. When the chemical activator is switched on, the detonation propagation becomes sustained. In the second simulation $E_a = 22RT_0$, two tests are again performed one with chemical activator and the other without. The chemical activator have no influence on the results as seen in Fig. 7. From these observations it can be inferred that chemical activation is needed for large heat release ($q = 50RT_0$) and small activation energies ($E_a \leqslant 10RT_0$). This explains why the shock indicator is a numerical issue in solid-phase detonations where the rate law (Vieille Law) depends mainly on the pressure and not on the temperature (the activation energy tends to zero).

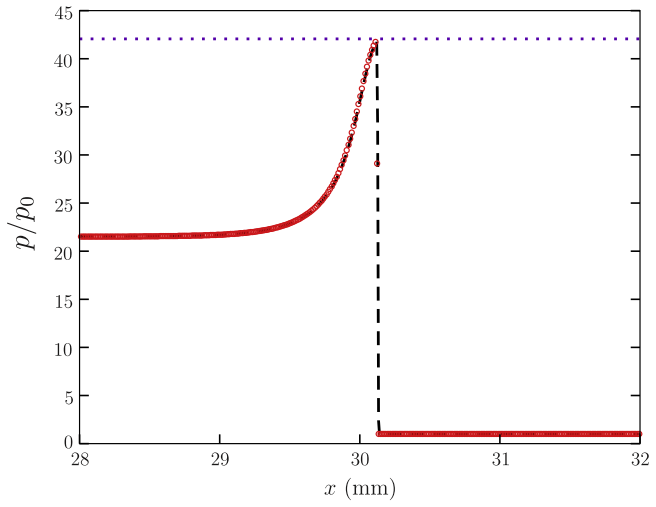


**Fig. 8.** Pressure profiles for test case ($A$) and $E_a/RT_0 = 22$ at $\Delta\chi_r = 4$ μm. Dashed line represents the solution obtained with uniform grid mesh and circles solution given by using a mapping function. Horizontal dotted line represents the von-Neumann state.

**Table 2**
Numerical resolution and corresponding grid points in the half reaction zone.

| $\Delta\chi_{min}$ (μm) | 16 | 8 | 4 | 2 | 1 |
|---|---|---|---|---|---|
| $N_{1/2}$ for $E_a = 22RT_0$ | 17 | 34 | 68 | 137 | 274 |
| $N_{1/2}$ for $E_a = 27RT_0$ | 16 | 33 | 66 | 132 | 265 |

### 4.4. Influence of the mapping function

In order to evaluate the validity of results given by the mapping function a test case is conducted by simulating an ideal stable detonation ($A$) for $E_a = 22RT_0$. A comparison between simulation obtained with an uniformly spaced grid and results obtained with mesh refinement is done. As it can be seen from Fig. 8 results computed with mesh refinement are in perfect accordance with those obtained with uniformly spaced grid. Moreover, the simulation running with mesh refinement is less time consuming. Indeed, simulation computed with mesh refinement is about 3.63 times faster than the simulation made with a uniformly grid spacing.

### 4.5. Influence of the mesh resolution

In this section, the needed resolution to correctly capture the dynamics of the wave front is studied. The different numerical resolutions used and their corresponding points, $N_{1/2}$, on the steady half reaction zone are given in Table 2. The pressure profiles for $\Delta\chi_r = 16$ μm, $\Delta\chi_r = 8$ μm, $\Delta\chi_r = 4$ μm, $\Delta\chi_r = 2$ μm and $\Delta\chi_r = 1$ μm is shown in Fig. 9 for case ($A$) at $E_a = 22RT_0$. Good agreement is found in term of global features. An enlargement

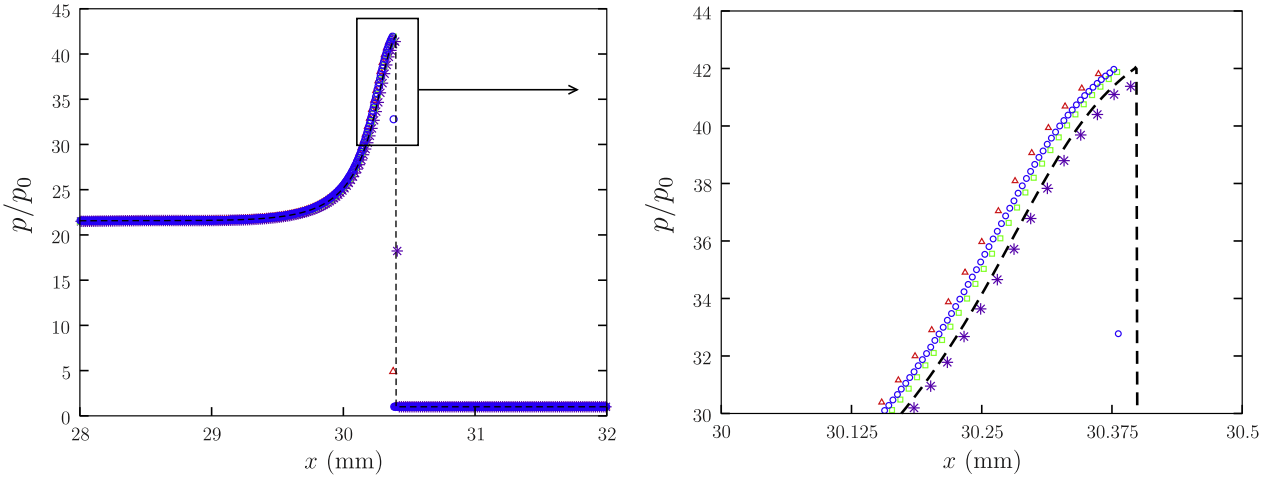


**Fig. 9.** Pressure profiles for test case (*A*) and $E_a/RT_0 = 22$ at: $\Delta\chi_r = 16$ μm (star), $\Delta\chi_r = 8$ μm (triangle up), $\Delta\chi_r = 4$ μm (square), $\Delta\chi_r = 2$ μm (circle) and $\Delta\chi_r = 1$ μm (dotted line). At right, enlargement of the pressure profiles.

**Table 3**
Convergence rates ($E_a/RT_0 = 22$). Subscripts VN and HRL denote von-Neumann state and the state where half of the reactant is consumed, respectively. $\mathcal{E}$ and $r$ denote the relative error and the convergence rate, respectively.

| $\Delta\chi_{min}$ (μm) | 16 | 8 | 4 | 2 | 1 |
|---|---|---|---|---|---|
| $\mathcal{E}_{VN}$ ($\times 10^{-2}$) | 1.620 | 0.590 | 0.290 | 0.150 | 0.070 |
| $\mathcal{E}_{HLR}$ ($\times 10^{-2}$) | 0.453 | 1.060 | 0.549 | 0.286 | 0.132 |
| $r_{VN}$ | – | 1.450 | 1.024 | 0.951 | 1.099 |
| $r_{HRL}$ | – | – | 0.949 | 0.941 | 1.115 |

**Table 4**
Relative error. $p_{max}$ is the maximum pressure recorded. $\mathcal{E}$ is the relative error and $r$ the convergence rate. $E_a/RT_0 = 27.82$.

| $\Delta\chi_{min}$ (μm) | 16 | 8 | 4 | 2 |
|---|---|---|---|---|
| $p_{max}/p_0$ | 60.6782 | 65.8143 | 67.2961 | 68.2065 |
| $\mathcal{E}$ ($\times 10^{-2}$) | 11.037 | 3.507 | 1.335 | – |
| $r$ | – | 1.654 | 1.393 | – |

view shows relative differences at the von-Neumann peak. We measured the relative errors during time evolution to estimate the order of convergence at the von-Neumann peak. The order of convergence, $r$, is given by

$$r = \frac{\log[\mathcal{E}^{\Delta'}/\mathcal{E}^{\Delta}]}{\log[\Delta'/\Delta]} \tag{24}$$

where $\mathcal{E}^{\Delta}$ and $\mathcal{E}^{\Delta'}$ are the errors using the mesh of numerical resolution $\Delta$ and its double $\Delta'$, respectively. Results obtained are summarized in Table 3. We find a convergence rate of approximately 1 at the von-Neumann state as expected. A convergence rate of approximately one is also found at half of the reaction zone. Note that the exact solutions are given by the steady ZND solution.

The influence of the numerical resolution on the results is also estimated using time-series data obtained from computations running with $\Delta\chi_r = 16$ μm, $\Delta\chi_r = 8$ μm, $\Delta\chi_r = 4$ μm and $\Delta\chi_r = 2$ μm for $E_a/RT_0 = 27.82$ in the case of ideal detonation (*A*). Results are depicted in Fig. 10. Data generated using the two lowest numerical resolutions show that the maximum peak of the shock pressure is under-estimated. For the two highest numerical resolutions, a converged solution is obtained as shown in Table 4. This means that an effective numerical resolution of 4 μm is enough to ensure that the detailed features of the pulsating wave are properly resolved. We can note that the rate of convergence is around 1.5. Note that a res-

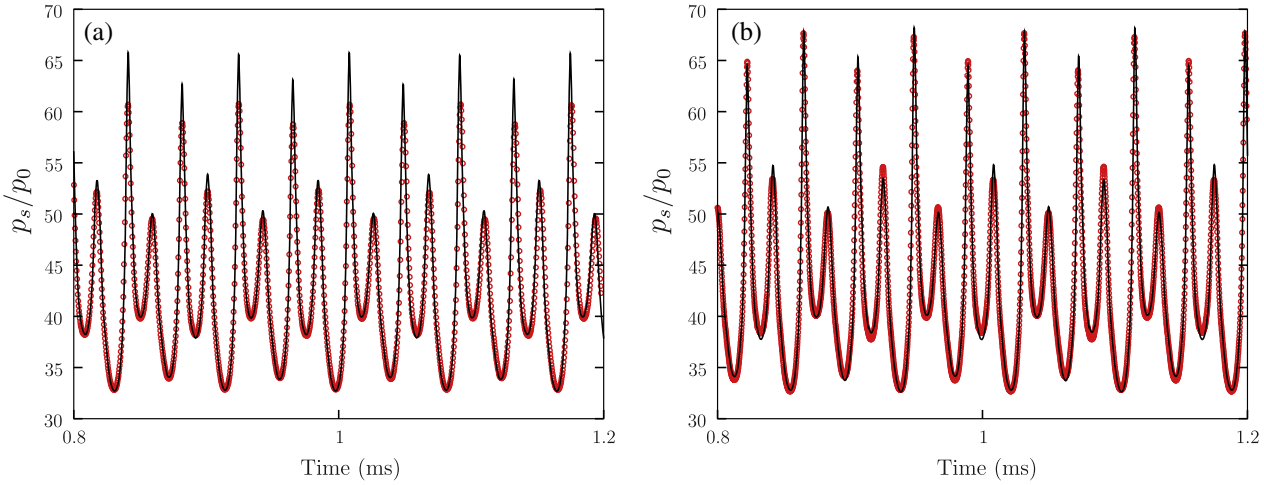


**Fig. 10.** Eight-period oscillations corresponding to $E_a = 27.82RT_0$ for different numerical grid resolutions. (a) $\Delta\chi_r = 16$ μm (symbol) and $\Delta\chi_r = 8$ μm (line). (b) $\Delta\chi_r = 4$ μm (symbol) and $\Delta\chi_r = 2$ μm (line).

**Table 5**
Critical steady ZND detonation velocity, $D_{cr}$, for different skin friction at $E_a = 22RT_0$.

| Law | Schlichting | Blasius | Colebrook | Prandtl | Constant |
|---|---|---|---|---|---|
| $D_{cr}/D_{CJ}$ | 0.7653 | 0.7631 | 0.7711 | 0.7663 | 0.7631 |

olution of 4 μm corresponds to 66 points per half ZND reaction zone length, $x_{1/2}$. The half-reaction zone length of the steady ZND detonation is usually defined as the distance at which half of reactants' fractions is consumed in ideal detonations. In this paper, unless specification an effective resolution of 66 points per half reaction zone is at least used in the numerical simulations. Furthermore, the analysis are carried out for stable or mildly unstable detonation, i.e. detonation having no more than sixteen-period oscillation.

### 4.6. Influence of the diameter reduction

Here, the importance of friction and heat losses on the detonation velocity deficit is investigated. Before all, determining the skin friction $c_f$ (that appears in the volumetric drag forces $f$) behind the leading wave is a severe task. In the literature, there exists several $c_f$ laws relating it to, the nature of the flow, the geometry, the roughness and the Reynolds number. Some authors [10,38] for a sake of simplification assumed the skin friction to be constant. Others authors like Zel'dovich and Kompaneets [8], Zhang and Lee [9] used the Blasius law to model the skin friction. Following the above authors, a study is conducted using different skin friction laws for a purpose of comparison. A Schlichting, Blasius, Colebrook, Prandtl [39] and constant $c_f$ laws defined respectively by

$$c_f = (2\log_{10}(Re_d - 0.65))^{-2.3} \quad (25)$$

$$c_f = 0.3164/Re_d^{-2.3} \quad (26)$$

$$c_f = (1.8\log_{10}(Re_d/6.9))^{-2} \quad (27)$$

$$c_f = 0.37(\log_{10}(Re_d))^{-2.584} \quad (28)$$

$$c_f = \text{constant} \quad (29)$$

are tested, see Table 5, where $Re_d = \rho v d/\mu$ is the Reynolds number, $v$ is the velocity in the laboratory frame and $\mu$ the viscosity coefficient determined according to the Sutherland's law. Computations are performed using the steady ZND equation with friction alone and $E_a = 22RT_0$. Results indicate that the critical velocity $D_{cr}$, defined here as the velocity below which the steady ZND equations does not have a solution, has approximately the same value that is $D_{cr}/D_{CJ} \approx 0.76$ despite the fact that the corresponding critical diameters differ from one law to another. In the remainder of the paper, the Blasius law is used in the numerical computations.

**Table 6**
Number of modes for $E_a/RT_0 = 22$; – and 0 means failure of detonation and stable detonation, respectively.

| Diameter (μm) | 150 | 155 | 180 | 200 | 220 | 280 | 300 | 900 |
|---|---|---|---|---|---|---|---|---|
| Period modes in case ($B$) | 2 | 1 | 1 | 0 | 0 | 0 | 0 | 0 |
| Period modes in case ($C$) | – | – | – | 2 | 1 | 0 | 0 | 0 |

We study now the detonation velocity deficit from the numerical results. Fig. 11 shows the detonation velocity as a function of the diameter. This figure illustrates the velocity deficit of the leading wave with the diameter reduction, i.e. with the increase of wall dissipative effects. In general, when heat losses are present, i.e. case ($C$), the deficit of velocity is naturally high compared to the adiabatic case, ($B$). For $E_a/RT_0 = 22$, fluctuations begin to appear at $d = 0.15$ mm in the adiabatic case and at a higher diameter, $d = 0.2$ mm, when heat losses are taken into account. Table 6 summarizes the period oscillation obtain in both cases ($B$) and ($C$) for $E_a/RT_0 = 22$. As it can be seen from Fig. 11 left, the points where oscillations are present are marked by a deviation of the mean solution from the steady laminar solution. Moreover, when the activation energy increases from $22RT_0$ to $27RT_0$, the detonation is always unstable even in the case of ideal detonations [2]. In this case (see Fig. 11 right), the mean solution always deviates from the prediction of the laminar steady detonation. It can be also noted that, fluctuations are an additional source of energy loss.

Now, we evaluate the influence of heat losses on the sonic locus. The former is determined by two means: the Master Equation of the steady ZND solution, Eq. (4), and the Master Equation of the Favre averaged equations, Eq. (7). First, an adiabatic test case is considered, i.e. $\dot{q}_{th} = 0$, for a validation step. It has a diameter $d = 0.2$ mm and $E_a/RT_0 = 22$. This case corresponds to a stable detonation (see Table 6). Since no fluctuation is present, the steady ZND solution and the mean solution are in perfect accordance as reported in Fig. 12. After, the mean sonic locus is evaluated for $d = 0.2$ mm and $E_a/RT_0 = 22$ in case ($C$). The result is also shown in Fig. 12. It can be seen that, heat losses lengthen the mean sub-

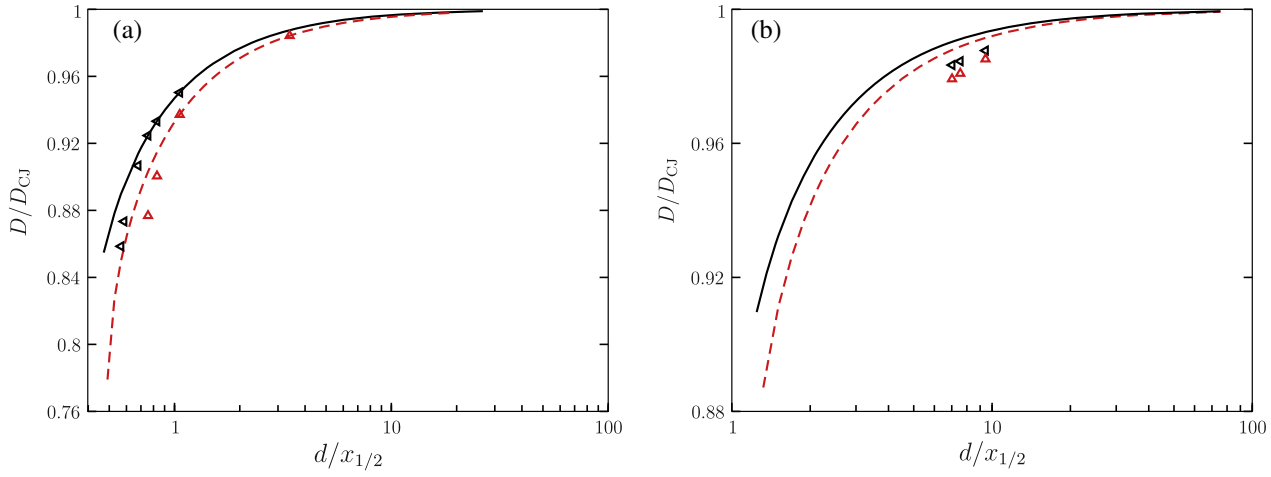


**Fig. 11.** Comparison between mean detonation velocity (symbols) and ZND solution (lines) for cases ($B$) and ($C$). Solid line and triangle left correspond to case ($B$). Dashed line and triangle up correspond to case ($C$). (a) $E_a/RT_0 = 22$. (b) $E_a/RT_0 = 27$. Results are scaled by $D_{CJ} = 1179.43$ m/s and $x_{1/2} = 0.265$mm.

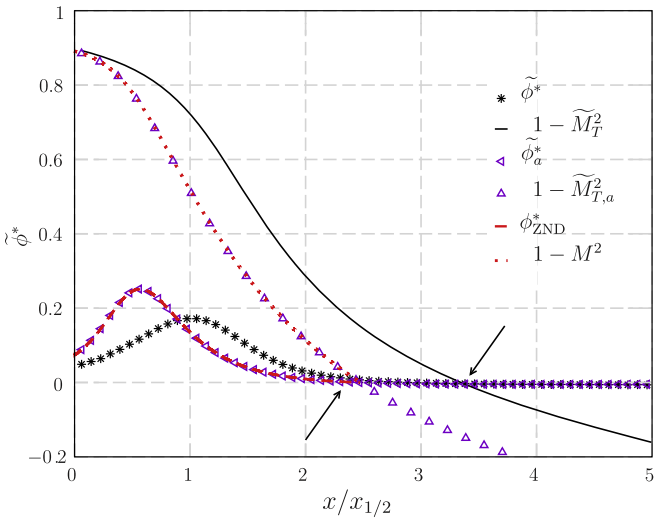


**Fig. 12.** Spatial distributions of dimensionless thermicity $\widetilde{\phi}^* = \phi x_{1/2}/\rho c^2 D_{\mathrm{CJ}}$ and Mach number functions $(1-M^2)$, $\left(1-\widetilde{M}_{T,a}^2\right)$ and $\left(1-\widetilde{M}_T^2\right)$. Subscript $a$ is for adiabatic case. Arrows indicate the locus of the mean sonic points. Cases $(B)$ and $(C)$ at $d = 0.2$ mm for $E_a/RT_0 = 22$.

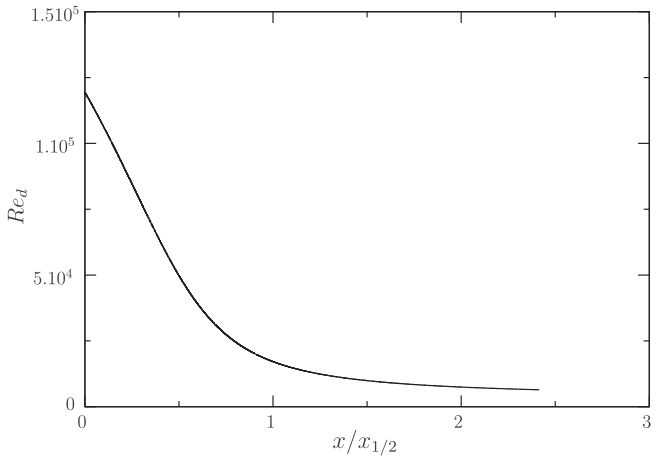


**Fig. 13.** Spatial distributions of the Reynolds number $Re$ behind the detonation front. Solution given by the ZND solver. Case $(C)$ at $d = 0.2$ mm and $E_a/RT_0 = 22$.

sonic reaction zone. The Reynolds number ($Re_d = \rho v d/\mu$, $v$ velocity in the laboratory frame) corresponding to the above case is plotted in Fig. 13 as a function of the distance to the shock. The Reynolds number reaches its maximum value at the shock and decreases as the reaction proceeds.

Fig. 14 gives plots of the shock pressure versus time at $d = 2$ mm and $E_a/RT_0 = 27$ for configurations $(B)$ and $(C)$. In the first test, the heat losses are switched off (Fig. 14 left). In the second one, they are switched on (Fig. 14 right). When heat losses are vanished, one predicts a period-two oscillation. But, when the heat losses are activated, the system undergoes period-four oscillations. The peak amplitudes are used to define the oscillation periods as indicated by the doted lines. This means that heat losses act like an activation energy increase in ideal detonations. This can be explained by the fact that heat losses at the wall tend to cool the flow as it enters the thermal boundary layer at the vicinity off the wall reducing thereby the temperature of the flow. This fact, leads in turn to an increase of the global activation energy $E_a/RT$.

If the diameter is further decreased, the effective activation energy increases due to the combined effects of both friction and heat losses. Period-eight oscillation is observed at $d = 1.86$ mm as reported in Fig. 15. Further decrease of the diameter to

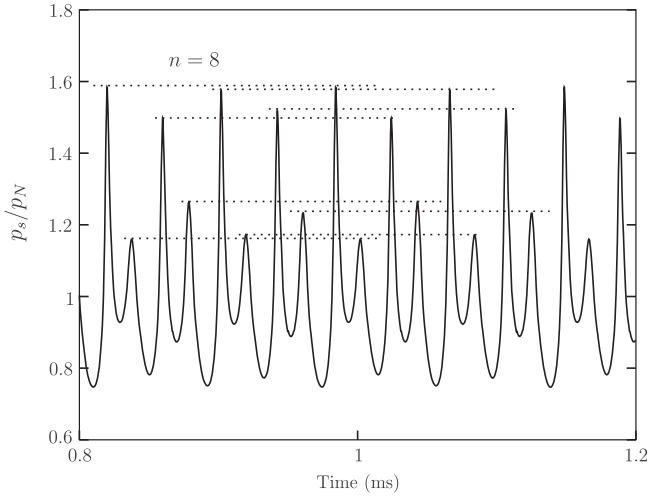


**Fig. 15.** Shock pressure $p_s$ histories for case $(B)$ at $d = 1.86$ mm and $E_a/RT_0 = 27$. $n$ is the number of period, $p_N$ is the von-Neumann pressure in deal case.

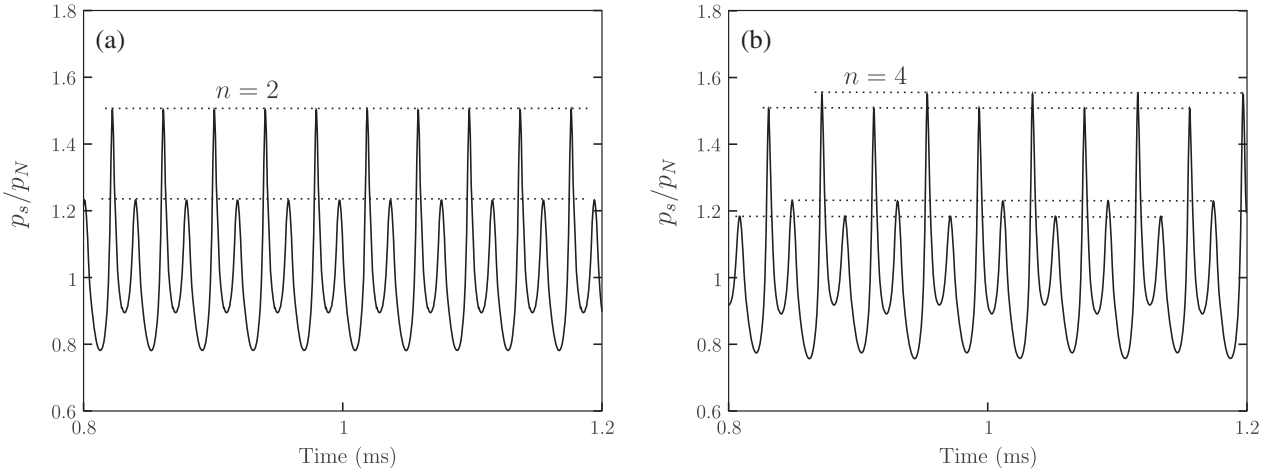


**Fig. 14.** Shock pressure $p_s$ histories at $d = 2$ mm and $E_a/RT_0 = 27$. (a) Test case $(B)$. (b) Test case $(C)$. $n$ is the number of period, $p_N$ is the von-Neumann pressure in the deal case.

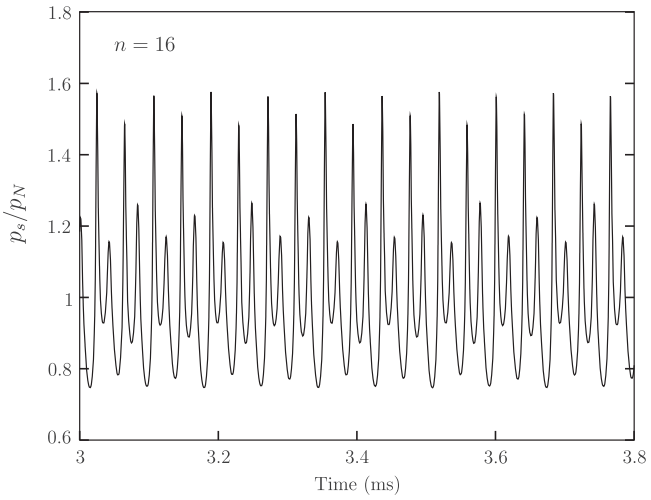


**Fig. 16.** Shock pressure $p_s$ histories for test case ($B$) at $d = 1.84$ mm and $E_a/RT_0 = 27$.

1.84 mm leads to period-sixteen oscillation as shown in Fig. 16. However, it is quite difficult to distinguish the maximum peak amplitudes. When the diameter is further decreased in the case of $E_a/RT_0 = 27$ the number of modes excited increases rapidly. The resolution required to capture the dynamics of the shock becomes increasingly overwhelming [4,13]. These points are out of scope of the current study.

Note that the smallest diameters considered in this paper for unsteady solution are 0.15 mm and 1.84 mm for $E_a/RT_0 = 22$ and $E_a/RT_0 = 27$, respectively.

## 5. Concluding remarks

In this paper, the analysis of the influence of momentum and heat losses on one-dimensional mildly unstable detonation is studied. First, it is found that heat losses affect the dynamics of the shock front, suggesting the possibility that the effective activation energy is increased. Moreover, the non-adiabatic influence is observed to increase the velocity deficit. This in turn slow down the rate of the reaction, leading thereby to the delay of the sonic point. The delay of the sonic surface is also observed to be fluctuations dependent. Furthermore, the present study demonstrated that similar results to those obtained in ideal detonation when the activation energy increases, can be predicted when the diameter decreases.

The results indicate that, shock-capturing coupled with fifth-order spatial discretization and third-order time discretization can gives accurate results in the case of mildly unstable detonation. The order of the numerical results is slightly greater than one, even for the case of mildly unstable non-ideal detonations. Moreover, the computations results show that the use of chemical activator is needed for large heat release and small activation energies. The proposed averaged method giving the mean sonic locus will be extended to two dimensional detonations.

## References

[1] Fickett W, Davis W. Detonation, theory and experiment. New York: Dover Publications; 1979.
[2] Lee J. The detonation phenomenon. Cambridge University Press; 2008.
[3] Kasimov A, Stewart D. On the dynamics of self-sustained one-dimensional detonations: a numerical study in the shock-attached frame. Phys Fluids 2004;16(10):3566–78.
[4] Ng H, Higgins A, Kiyanda C, Radulescu M, Lee J, Bates K, et al. Nonlinear dynamics and chaos analysis of one-dimensional pulsating detonations. Combust Theory Modell 2005;9:159–70.
[5] Abderrahmane H, Paquet F, Ng H. Applying nonlinear dynamic theory to one-dimensional pulsating detonations. Combust Theory Modell 2011;15(2):205–25.
[6] Hwang P, Fedkiw R, Merriman B, Aslam T, Karagozian A, Osher S. Numerical resolution of pulsating detonation waves. Combust Theory Modell 2000;4(3):217–40.
[7] Sharpe G. Linear stability of idealized detonations. Proc Roy Soc Lond Ser A: Math Phys Eng Sci 1997;453(1967):2603–25.
[8] Zel'dovich Y, Kompaneets A. Theory of detonation. Academic Press; 1960.
[9] Zhang F, Lee J. Friction-induced oscillatory behavior of one-dimensional detonations. Proc Roy Soc Lond A 1994;446:87–105.
[10] Dionne J-P, Ng H, Lee J. Transient development of friction-induced low-velocity detonations. Proc Combust Inst 2000;28:45–651.
[11] Higgins A. Shock wave science and technology reference library. Detonation dynamics, vol. 6. Berlin Heidelberg: Springer-Verlag; 2012. p. 33–105 [Ch. Steady one-dimensional detonations].
[12] Chinnayya A, Hadjadj A, Ngomo D. Computational study of detonation wave propagation in narrow channels. Phys Fluids 2013;25:036101.
[13] Romick C, Aslam T, Powers J. The effect of diffusion on the dynamics of unsteady detonations. J Fluid Mech 2012;699:453–64.
[14] Henrick A, Aslam T, Powers J. Simulations of pulsating one-dimensional detonations with true fifth order accuracy. J Comput Phys 2006;213:311–29.
[15] Bourlioux A, Majda AJ, Roytburd V. Theoretical and numerical structure for unstable one-dimensional detonations. SIAM J Appl Math 1991;51(2):303–43.
[16] Sharpe G, Falle S. Numerical simulations of pulsating detonations: I. Nonlinear stability of steady detonations. Combust Theory Modell 2000;4:557–74.
[17] Colella P. Multidimensional upwind methods for hyperbolic conservation laws. J Comput Phys 1990;87(1):171–200.
[18] Quirk J. Godunov-type schemes applied to detonation flows. Tech. rep. DTIC Document, ICASE/ NASA CR 191447. Report no. 93-15; 1993.
[19] Yee H, Kotov D, Wang W, Shu C-W. Spurious behavior of shock-capturing methods by the fractional step approach: problems containing stiff source terms and discontinuities. J Comput Phys 2013;241:266–91.
[20] Chinnayya A, LeRoux A-Y, Seguin N. A well-balanced numerical scheme for the approximation of the shallow-water equations with topography: the resonance phenomenon. Int J Finite Volumes 2004;1:1–33.
[21] Menikoff R, Shaw M. Reactive burn models and ignition & growth concept. In: Soulard L, editor. EPJ web of conferences, new models and hydrocodes for shock wave processes in condensed matter, vol. 10. EDP Sciences; 2010. p. 00003.
[22] Fryxell B, Muller E, Arnett W. Hydrodynamics and nuclear burning. Tech. rep. Garching: Max Planck Institut fur Astrophysik; 1989 [preprint MPA449].
[23] Papatheodore TL, Messer OB. On numerical considerations for modeling reactive astrophysical shocks. Astrophys J 2014;782(1):12.
[24] Timmes F, Zingale M, Olson K, Fryxell B, Ricker P, Calder A, et al. On the cellular structure of carbon detonations. Astrophys J 2000;543(2):938.
[25] Nikolaev Y, Zak D. Quasi-one-dimensional model of self-sustaining multifront gas detonation with losses and turbulence taken into account. Combust Explos Shock Waves 1989;25(2):225–33.
[26] Zhang F, Chue R, Lee J, Klein R. A nonlinear oscillator concept for one-dimensional pulsating detonations. Shock Waves 1998;8(6):351–9.
[27] Xu S, Aslam T, Stewart D. High resolution numerical simulation of ideal and non-ideal compressible reacting flows with embedded internal boundaries. Combust Theory Modell 1997;1(1):113–42.
[28] Gamezo V, Desbordes D, Oran E. Formation and evolution of two-dimensional cellular detonations. Combust Flame 1999;116(1–3):154–65.
[29] Radulescu M, Sharpe G, Law C, Lee J. The hydrodynamic structure of unstable cellular detonations. J Fluid Mech 2007;580:31–81.
[30] Sow A, Chinnayya A, Hadjadj A. Mean structure of one-dimensional unstable detonation with friction. J Fluid Mech 2014;743:503–33.
[31] Ngomo D, Chaudhuri A, Chinnayya A, Hadjadj A. Numerical study of shock propagation and attenuation in narrow tubes including friction and heat losses. Comput Fluids 2010;39(9):1711–21.
[32] Chinnayya A, Daniel E, Saurel R. Modelling detonation waves in heterogeneous energetic materials. J Comput Phys 2004;196(2):490–538.
[33] Shu C-W. Essentially non-oscillatory and weighted essentially non-oscillatory schemes for hyperbolic conservation laws. Cr-97-206253 icase report. no. 97-65, NASA; 1997.
[34] Chaudhuri A, Hadjadj A, Chinnayya A, Palerm S. Numerical study of compressible mixing layers using high-order WENO schemes. J Sci Comput 2011;47(2):170–97.
[35] Mott DR, Oran ES, van Leer B. A quasi-steady-state solver for the stiff ordinary differential equations of reaction kinetics. J Comput Phys 2000;164(2):407–28.
[36] Anderson D, Tannehill J, Pletcher RH. Computational fluid mechanics and heat transfer. New York, NY: Hemisphere Publishing; 1984.
[37] Petitpas F, Saurel R, Franquet E, Chinnayya A. Modelling detonation waves in condensed energetic materials: multiphase CJ conditions and multidimensional computations. Shock Waves 2009;19(5):377–401.
[38] Sivashinsky GI. Combustion in hydraulically resisted flows. Rev Roy Acad Cien Ser A: Mater 2007;101(2):173–86.
[39] Schlichting H, Gersten K, Gersten K. Boundary-layer theory. Springer; 2000.